# Optimal charging set point for a latent thermal energy storage for cold chain transport

*Wim Beyne[a,b], Kenny Couvreur[a,b,c], Steven Lecompte[a,b] and Michel De Paepe[a,b]*

[a] *Department of Electromechanical, Systems and Metal Engineering - UGent, Ghent , Belgium, wim.beyne@ugent.be*
[b] *FlandersMake@UGent – Core lab EEDT - MP, Leuven, Belgium, www.flandersmake.be,*
[c] *Institution, City, Country*
[c] *Research group Thermal energy in industry, Ghent University, Kortrijk, Belgium*

**Abstract:**
Cold chain transport is a major contributor to greenhouse gas emissions worldwide. To reduce costs and failure rates, passive transport utilizing latent thermal energy storage can be applied instead of active transport containers. The energy storage needs to be pre-charged before transport and therefore an effective charging strategy is key. The present article discusses a thermal battery design and characterizes the charging time of the battery as a function of heat transfer fluid mass flow rate and temperature. Subsequently it discusses the optimum working point for charging the battery taking into account both the energy cost and the wage of idling workers during charging. The optimal point depends heavily on the size of the system, where small systems require minimizing idle time while larger systems require a balance between energy and time.

**Keywords:**
Cold chain transport, Latent Thermal energy storage, Cost optimization.

# 1. Introduction

Cold chain transport accounts for 2.5 % of the global greenhouse gas emissions [1] and between 40 % and 60 % of energy use in supermarkets [2]. Most commonly used systems apply active refrigeration systems which employ an on board chiller during transport. As a result, these systems are susceptible to blackouts, cause vibrations and there is a possibility of refrigerant leakage [3].

To prevent the mentioned issues, a latent thermal energy storage (LTES) can be applied to maintain the cold chain. The temperature is maintained by use of phase change materials (PCMs) which are chilled prior to transportation. Liu et al. showed that a passive system can reduce cost by half compared to active systems [4].

Due to the high potential, much effort has gone into studying the transport phase of cold storages with LTES [5-9]. All these studies employed PCM packages which where solidified prior to the experiment. No attention was paid as to how the thermal batteries where charged.

A charging time of the LTES higher than the loading and unloading time increases cost. Either through idle time for both equipment and operators as the storages are charged or because excess LTES needs to be acquired for pre-charging and stockpiling. The additional costs can be avoided by designing the battery to minimize the charging time.

In this article, a plug-in thermal battery is presented and experimentally tested. In an experimental analysis, the charging time of the battery is evaluated as a function of the heat transfer fluid settings. In the economic analysis, the optimum cycle set point as a function of economic parameters and system size is investigated.

# 2. Methods

## 2.1. Experimental setup and measurement procedure

The battery is formed using an extruded aluminium profile with a cross section as shown in Fig. 2. The channels labelled with an A are filled with metal foam enhanced PCM and closed. In contrast, the channels labelled with a B are not closed and used as flow passages for the HTF. The channel labelled C is used to connect two profiles by sliding the protruding edges into each other. The complete battery is shown in Fig. 1 with four extruded profiles welded together and two collectors fitted at the end of the profiles. The collectors allow the flow of HTF through each profile in the direction of the arrows. Two nipples are fitted at the in- and outlet of the HTF.

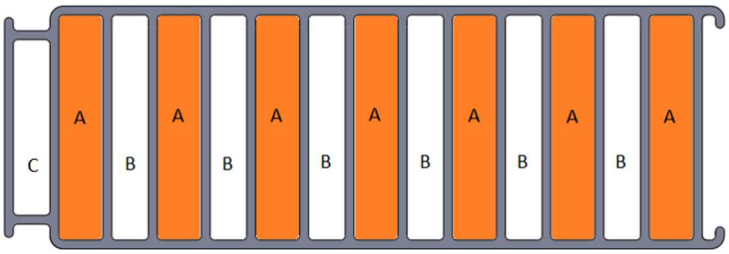


*Fig. 2: Cross section of the extruded profile. Channels labelled A are filled with PCM and closed. Channels labelled B are flow passages for the HTF and channels labelled C are left empty.*

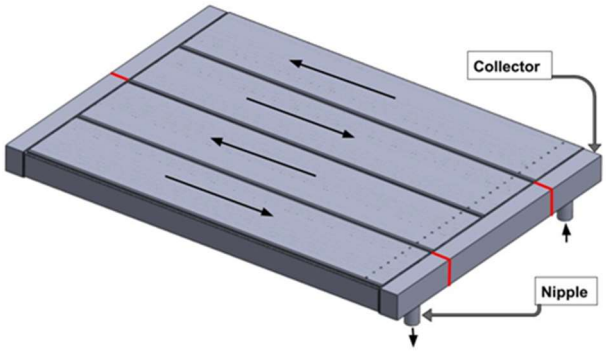


*Fig. 1: A CAD drawing of the battery with four extruded profiles, two collectors and two nipples for the in- and outflow of HTF. Arrows show the direction of the HTF flow for each extruded profile.*

The PCM channels are filled with a total of 8.074 kg of PCM RT 5 HC from Rubitherm [10]. The properties of the PCM are given in Table 1. The PCM is a mix of paraffin and therefore has a melting range rather than a single phase change temperature. The main peak of the latent heat is at 5 °C for the solidification and 6 °C for the melting.

*Table 1 Technical data of RT5HC as given by the manufacturer [10].*

| Property | Values | Units |
|---|---|---|
| Melting area | 5 – 6 (main peak at 6) | [ºC] |
| Congealing area | 6 – 5 (main peak at 5) | [ºC] |
| Heat storage capacity ±7.5% | 250 | [kJ/kg] |
| Specific heat capacity | 2 | [kJ/kg·ºC] |
| Density solid | 0.88 | [kg/l] |
| Density liquid | 0.76 | [kg/l] |
| Heat conductivity (both phases) | 0.2 | [W/m·ºC] |
| Volume expansion | 13 | [%] |

The HTF used for the experiments is Temper 30 [11]. The tabulated properties of the HTF are given by the manufacturer. The data is correlated using polynomial functions where the order is increased until the error of the correlation is smaller than the measurement error. The resulting correlations are given in Table 2. The HTF is cooled using a 3.5 kW chiller which controls the temperature of a vessel of HTF. The temperature of the vessel is set between 0 °C and 15 °C prior to the start of the experiment. The experiment starts by turning on the HTF pump (Grundfoss CR3-11). The pumps frequency is set in percentages of 50 Hz ranging from 25 % to 100 %.

*Table 2: Correlations for the thermal properties of the heat transfer fluid.*

| Property | Polynomial ( T in K) | Units |
|---|---|---|
| Thermal conductivity | 0.00128571 T + 0.11023571 | [W/mK] |
| Density | -0.00119047619 $T^2$ + 0.343214286 T + 1179.12116 | [kg/m³] |
| Specific heat capacity | -0.0285714286 $T^2$ + 18.6085714 T + 123.095071 | [J/kgK] |
| Dynamic viscosity | 1.68181818e-06 $T^4$ -0.00195422121 $T^3$ +0.853165748 $T^2$ - 165.921822 T+1.21346739e+04 | [mPa s] |

The mass flow and temperature are measured throughout the experiment. The mass flow is measured using a Krohne Optimass 1400C S25 with an accuracy of ± 0.15 % of the mass flow + 0.00075. The temperatures are measured using four K-type thermocouples, two at the inlet of the HTF and two at the outlet of the HTF which are averaged to determine the temperature of the HTF at the in- and outlet. The thermocouples are calibrated with an accuracy of ± 0.15 °C. The measurements are read using a Keithley 2700 multiplexer, a PC and Labview software. The sampling time $\Delta t_s$ is maximum 5.0 seconds.

The charging time $t_c$ is the time difference between the start of the experiment and the time at which the in- and outlet temperature of the HTF are equal. The error of the charging time consists of two contributions. Firstly, there is an error on the starting and end time due to the finite sampling time. Secondly, there is an uncertainty on the moment where the in- and outlet temperatures are equal due to the uncertainty of the thermocouple measurements. This uncertainty is the time difference between the moment where the HTF temperatures are not significantly different $t_e$ and the moment where the HTF measurement at in- and outlet are equal $t_c$. The error on the charging time can thus be written as Equation 1.

$$\varepsilon_{t_c} = \sqrt{{\Delta t_s}^2 + |t_c - t_e|^2} \qquad (1)$$

A total of 42 experiments are executed with pump frequencies varying between 25 % and 100 %. The average inlet condition is varied between 0 °C and -15 °C.

## 2.2. Economic analysis

The operational cost $c_{tot}$ of charging a battery system is comprised of two major parts as given in Equation 2. Firstly the energy cost of charging the battery system which is the factor the number of batteries, the energy used to charge the battery $E_{tot}$ and the electricity price $p_e$. Secondly, the cost of an idling driver while the battery is charged. This cost is the factor of the waiting time for the driver and the hourly wage of the driver $p_h$. The waiting time is the difference between the time to unload and load the transport container $t_l$ and the charging time of the battery. The waiting time cannot become negative.

$$c_{tot} = n_{bat}\, E_{tot}\, p_e + \max(t_c - t_l, 0)\, p_h \qquad (2)$$

The price of electricity is set at the average electricity price for non-household consumers for the euro-area in 2018: 0.12 €/kWh [12]. The hourly wage of the driver is set to the minimum wage of a driver in Belgium: 10.7 €/h [13].

The total energy used to charge the battery consists of two parts: the pumping energy $E_{pump}$ and the energy of the $E_{chiller}$. If multiple batteries are used for one container, the total energy is multiplied by the number of batteries $n_{bat}$ (Equation 3).

$$E_{tot} = E_{chill} + E_{pump} \quad (3)$$

The chiller energy is the electricity required to charge the battery from the initial temperature $T_{ini}$ to the set point temperature of the chiller $T_{set}$ . This energy consists of the HTF fluid energy, the aluminium energy and the PCM energy. Since the masses, specific heat and latent heat of the HTF, aluminium and PCM are known, the battery energy $E_{bat}$ can be written as Equation 4.

$$E_{bat} = m_{alu}\, c_{p,alu}(T_{ini} - T_{set}) + m_{HTF}\, c_{p,HTF}(T_{ini} - T_{set}) + m_{PCM}\, c_{p,PCM}(T_{ini} - T_{set}) + m_{PCM}\, h_{lat,PCM} \quad (4)$$

The energy of the chiller $E_{chiller}$ is the battery energy $E_{bat}$ divided by the coefficient of performance (COP) of the chiller $COP$. Only a single design point of the chiller is known, therefore a simplified model is used to predict the performance of the chiller. The model predicts the COP as the ratio of the real COP and the Carnot cycle COP in the nominal point times the Carnot cycle COP of the set point (see Equation 5). The model corresponds to one of the models proposed by Zweifel without the part load ratio correction [14].

$$COP = \left(\frac{COP_{real}}{COP_{Carno}}\right)_{nom} \frac{T_{set}}{T_{amb} - T_{set}} \quad (5)$$

The energy of the chiller $E_{chiller}$ can now be written as the battery energy $E_{bat}$ divided by the COP (Equation 6).

$$E_{chill} = {}^{E_{bat}}/_{COP} \quad (6)$$

The second part of the total energy is the energy required to pump the HTF: $E_{pump}$. It is the factor of the pressure drop $\Delta P$, the volume flow rate $q$, the pump and motor efficiency respectively $\eta_{pump}$ and $\eta_{motor}$ , and the charging time $t_c$ (Equation 7). The motor efficiency is assumed constant as given on the motor nameplate (82.7 %).

$$E_{pump} = \frac{\Delta P\, q}{\eta_{pump}\, \eta_{motor}}\, t_c \quad (7)$$

The pressure drop $\Delta P$ and volume flow rate $q$ are the result of the balance between the hydraulic circuit pressure drop and the pump pressure. Therefore both the pump and the hydraulic circuit need to be characterized. Grundfoss provides performance characteristics of pump and motor as a function of motor frequency in its product centre [15]. However, these characteristics can only be evaluated using the graphical user interface of Grundfoss. To allow integrating the characteristics into an economic optimization, an analytical form of the characteristics is developed. Furthermore, the induction motor used to determine the characteristics is not the induction motor installed at the setup. Therefore, characteristics should ultimately be based on rotational speed rather than on frequency supplied to the pump.

The pressure drop as a function of the volume flow rate for different pump frequencies is given by the online sizing tool of the manufacturer. A first possibility to fit the curves is to fit a second order polynomial for several frequencies. However, this would not allow to continuously vary the pump set point and would hinder the economic optimization. Therefore the pressure drop at secondary frequencies is scaled using the ratio of the shafts rotational speed of the base curve $n_{base}$ and the current rotation speed of the pump $n_f$ (Equation 8). The rotational speed of the base curve is given by the manufacturer as 3452 rpm. The rotational speed of the pump for each case depends on the

frequency and working point. Since only the frequency is given, the rotational speed of each case is not known.

$$\Delta P = \left(\frac{n_f}{n_{base}}\right)^2 \Delta P_{base}\left(q \Big/ \frac{n_f}{n_{base}}\right) \quad (8)$$

The pump is driven by an induction motor. Therefore the torque of the motor $T$ is a function of the slip speed of the rotor $s$. The torque-slip function is not given by the manufacturer, but is assumed to be linear for low slip values. With the torque known, the shaft power delivered by the rotor is calculated as the factor of the rotor speed and torque. By equating the required pumping power given by the manufacturer to the shaft power, the rotational speed of each set point can be determined. With the rotational speed known, the pressure drop of each case can be fitted to a single second order polynomial at the base speed ($\Delta P_{base}$ in Equation 8). The slope of the torque-slip function is found by minimizing the error between the pressure drop calculated by Equation 8 and the pressure drop given by the manufacturer. The resulting characteristics are given by Equation 9 and 10. The root mean square deviation is 1.1 % with a maximum deviation of 2.81 %.

$$T(s) = 495\ s \quad (9)$$

$$\Delta P_{base} = -4.146 \cdot 10^{11}\, q^2 + 1.695 \cdot 10^9\, q + 1.129 \cdot 10^6 \quad (10)$$

The efficiency of the pump can be characterized in a similar manner. First the efficiency $\eta_{pump}$ is scaled to the efficiency of the pump at the base speed $\eta_{base}$ by Equation 11.

$$\eta_{pump} = \eta_{base}\left(q \Big/ \frac{n_f}{n_{base}}\right) \quad (11)$$

Secondly the base efficiency is fitted to the data by a second order polynomial. The resulting function is shown in Equation 12. The root mean square deviation of the efficiency is 0.33 % with a maximum deviation of 0.85 %.

$$\eta_{base} = -5.064 \cdot 10^5\, q^2 + 9.546 \cdot 10^2\, q + 1.321 \cdot 10^{-1} \quad (12)$$

The pumping power is calculated as the factor of the pressure drop and the volume flow rate, divided by the pump efficiency. The correlation results in a root mean square deviation of 1.18 % and a maximum error of 2.70 %.

With the pump characteristics known as a function of the rotor speed, the induction motor needs to be characterized as well. The induction motor is characterized from the nominal power and speed given on the name plate. The resulting torque-slip function is given by Equation 13.

$$T(s) = 461.6\ s \quad (13)$$

The pressure drop of the battery circuit is not measured. However, for each measurement the frequency and volume flow rate are known. By equating the shaft power to the pump power, the working point can be determined for each measurement. The hydraulic circuit characteristic can then be fitted to Equation 14, where the constant $a$ fits the static head and $b$ fits the dynamic head.

$$\Delta P_c = a + b\, q^2 \quad (14)$$

# 3. Results

## 3.1. Charging time correlation

The charging time is measured for 42 settings of pump frequency and inlet temperature of the HTF. It is the time required to cool the battery from the initial temperature to the final temperature. Therefore it is inversely related to the average heat transfer rate. Between 42 to 62 % of the energy is stored in latent heat which is driven by the temperature difference between the HTF and the

solidification temperature of the PCM. Equation 13 is proposed to correlate the charging time tying the inverse relation to the average heat transfer rate and the dependency of the temperature difference together. Both the slope $f_s(\bar{\dot{m}})$ and the intercept $f_i(\bar{\dot{m}})$ are a function of the average mass flow rate $\bar{\dot{m}}$.

$$t_c = \frac{f_s(\bar{\dot{m}})}{(T_{pc} - T_{in})} + f_i(\bar{\dot{m}}) \quad (13)$$

The slope function is the ratio of the latent energy over the average heat transfer coefficient. The average heat transfer coefficient can be estimated using the effectiveness-number of transfer units method by assuming an isothermal solidification and averaging the overall heat transfer coefficient [16]. The resulting function is shown in Equation 14, with $s_1$ and $s_2$ being fitting coefficients.

$$f_s(\bar{\dot{m}}) = s_1 \frac{E_{lat}}{\varepsilon\, \bar{\dot{m}}\, c_p} + s_2 \quad (14)$$

The intercept bundles two effects. Firstly, it takes time for the cold HTF to fill the battery. During this time, only a part of the surface area in the battery is transferring heat and therefore this delays charging. It is estimated as the volume of the battery channels $V$ divided by the average mass flow rate $\bar{\dot{m}}$. A second effect is caused by the sensible heat of the battery not determined by the temperature difference between the phase change temperature of the PCM and the HTF inlet. It is fitted as an exponential function of the average mass flow rate with fitting coefficients $i_1$ and $i_2$.

$$f_i(\bar{\dot{m}}) = \frac{V}{\bar{\dot{m}}} + i_1 e^{i_2 \bar{\dot{m}}} \quad (15)$$

The result of fitting Equation 13-15 to the measurements correlates the charging time with a root mean square deviation of the correlation is 2.2 %.

The charging time of the battery in the operational range of the battery is shown on Fig. 3. The charging time varies between 342 s and 1552 s.

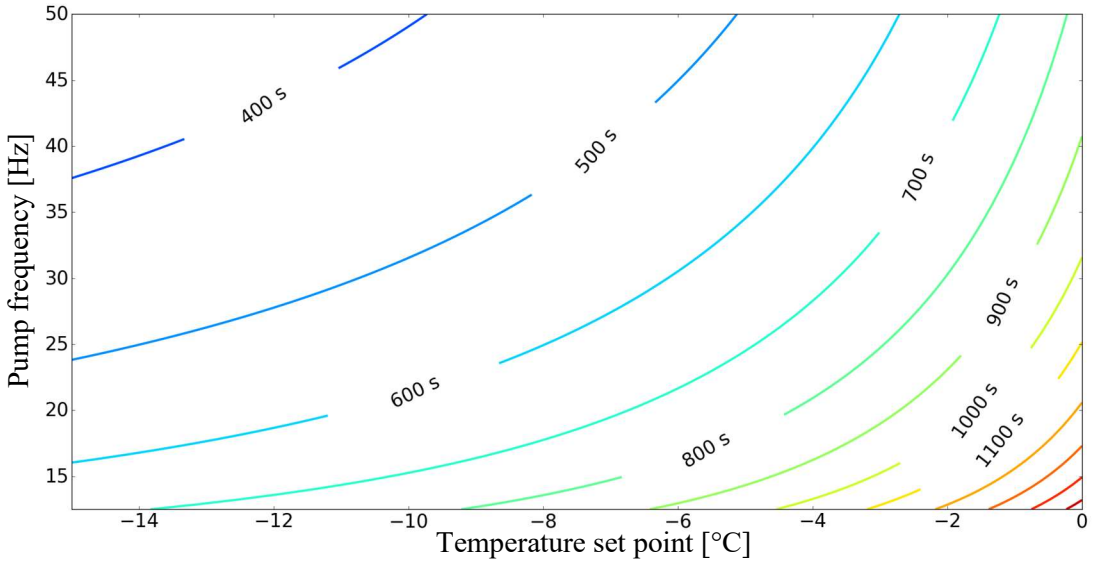


*Fig. 3: Charging time as a function of pump frequency and temperature set point.*

## 3.2. Hydraulic characterization

The pressure drop of each experiment is estimated using the torque-slip function of the induction motor (Equation 13) and the pump characteristics given by Equations 8, 10-12. The resulting correlation is shown in Fig. 4. The error bars on the pressure axis represent the error of the correlation, while the error bars on the volume flow rate are an experimental uncertainty. The root mean square deviation is 6.8 %.

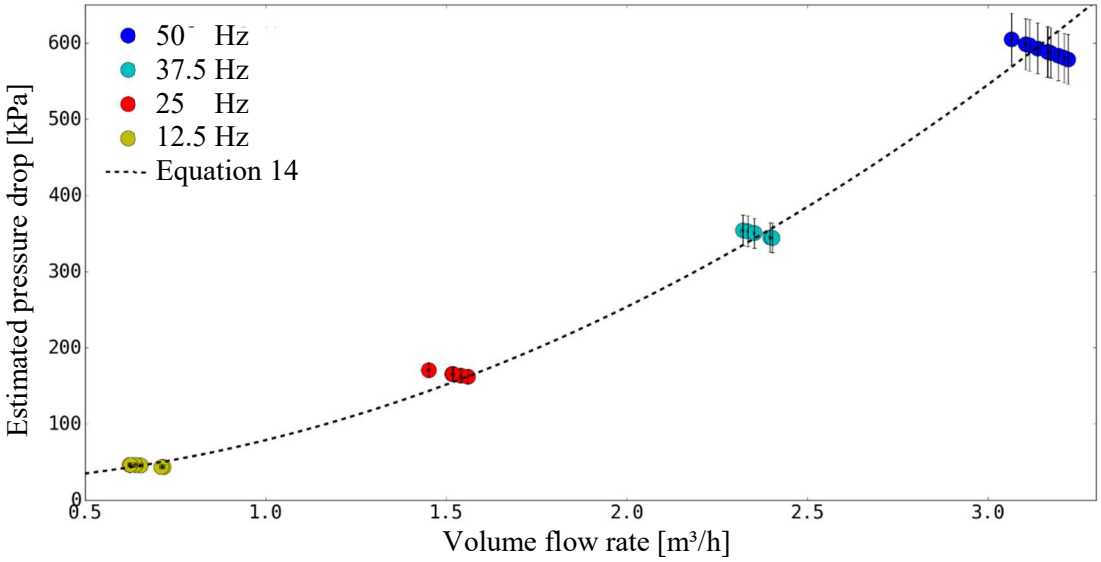


*Fig. 4: The estimated pressure drop versus measured volume flow rate for the experiments with the fitted characteristic with a=20.5 and b=58.3.*

## 3.3. Economic analysis

The total operational cost consists of the waiting cost and the energy cost which in term consist of the pumping energy and the chiller energy. The chiller energy according to Equation 4-6 only depends on the temperature set point of the charging. It varies between 925 kJ at 0°C and 2295 kJ at -15 °C for a single battery.

The pump power only depends on the chosen pump frequency. However, since the pump energy is the pump power multiplied by the charging time, the required energy varies with both inlet temperature and pump frequency. Fig. 6 shows a contour plot of the pump energy normalized to the maximum pump energy. The maximum of 897 kJ occurs at high pump frequencies and a low temperature set point. This is the result of the high pump power at higher frequencies and slow charging time due to the low temperature set point. The pump energy can be reduced almost entirely by decreasing both pump frequency and temperature set point, with reducing the pump frequency having the highest gradient.

The sum of the pump and the chiller energy is shown in Fig. 5. The minimum energy is found at the lowest pump frequency and highest temperature set point. The low temperature set point minimizes the energy required to chill the battery while the low pump frequency significantly reduces the pump energy.

Minimizing the energy cost maximizes the charging time of the battery which in turn maximizes the waiting cost. Optimizing the settings is thus a balance between the energy cost and the personnel cost. Increasing the number of batteries in a single transport, increases the energy cost but does not increase the personnel cost since multiple pumps can be applied in parallel. As a result, the balance of the energy and personnel cost is shifted. Therefore the cost analysis is made for three different system sizes.

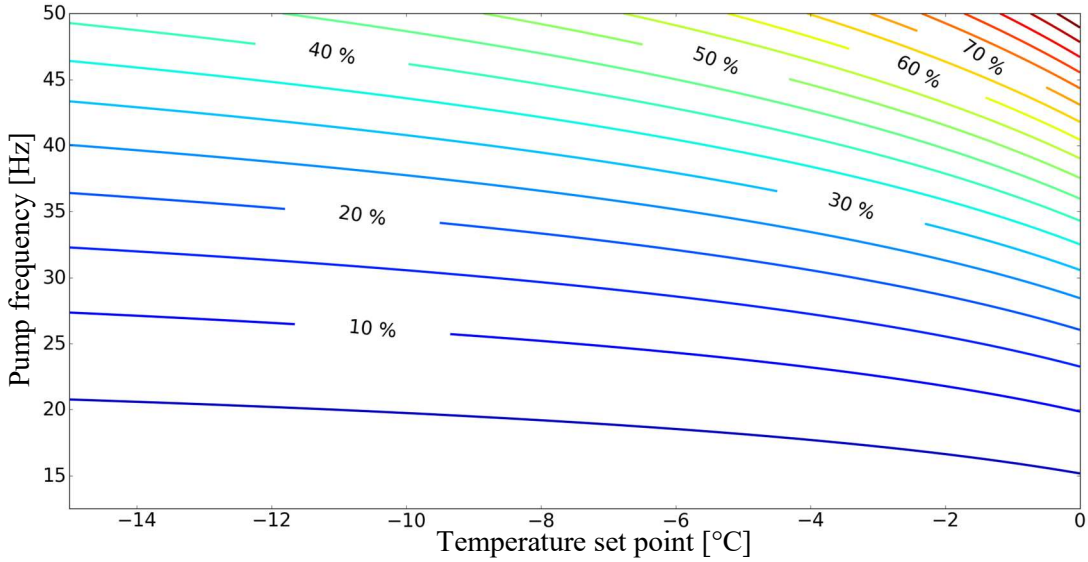


*Fig. 6: Contour of the pump energy a battery system expressed as a percentage of the maximum value as a function of temperature set point and pump frequency.*

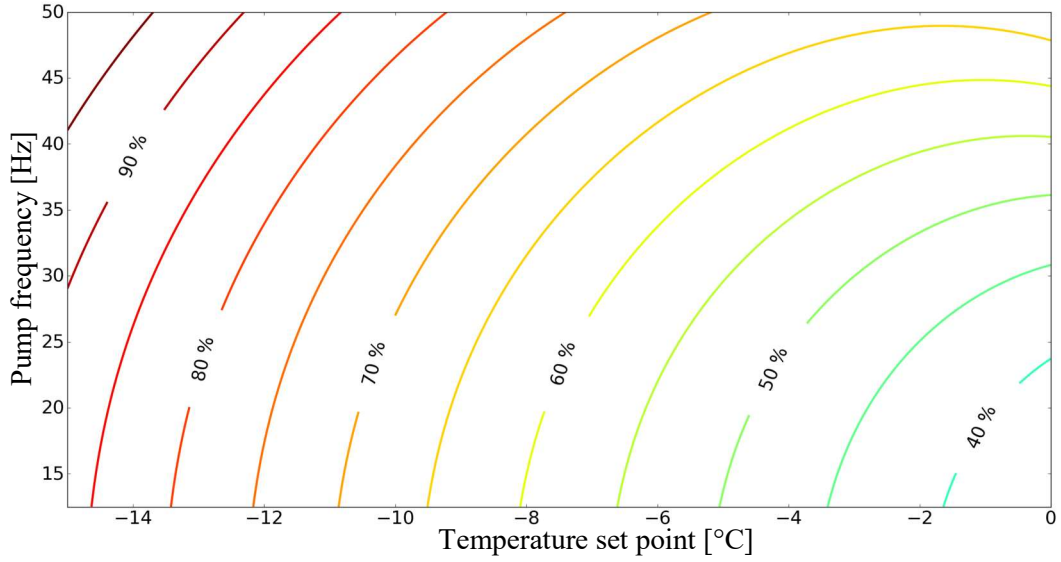


*Fig. 5: Contour of the total energy of a battery system expressed as a percentage of the maximum value as a function of temperature set point and pump frequency.*

**Case I: single battery**

For a single battery, the personnel cost is dominant over the energy cost in the case of a single battery. As a result, the contour plot of the total cost shown in Fig. 7 resembles the contour plot of the charging time. The minimum cost is found at 24 % of the maximum cost for the highest pump frequency and lowest temperature. In this optimum, the energy only comprises 8.7 % of the total cost. If the waiting time is included, the optimal charging time will only be slightly higher than the waiting time. However, the difference with the fastest charging set point is only a couple percentage points compared to the maximum cost. This is the result of the low energy cost compared to personnel cost for a single battery system.

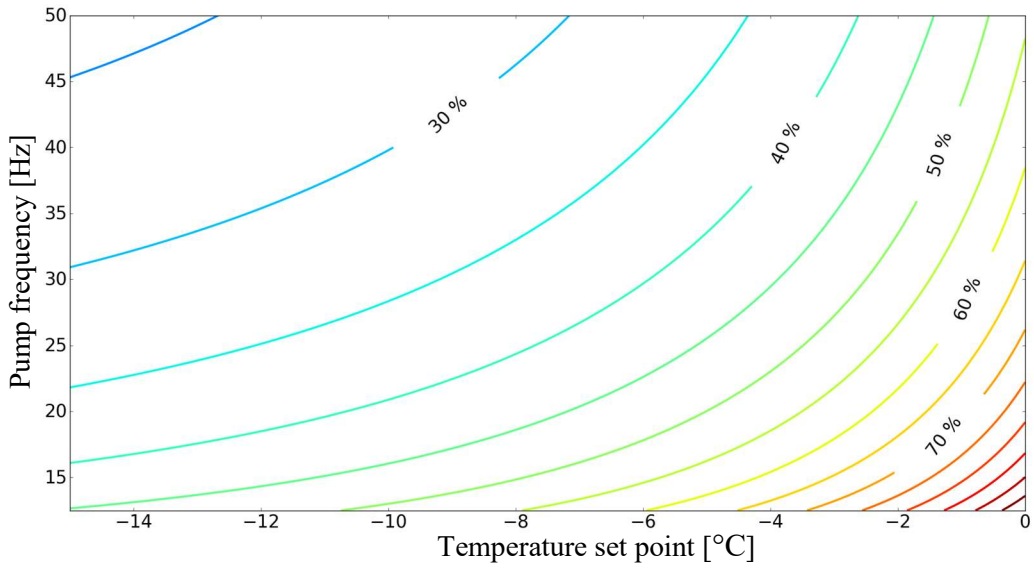


*Fig. 7: Contour of the total cost of a battery system with a single battery expressed as a percentage of the maximum value as a function of temperature set point and pump frequency.*

**Case II: ten batteries**

For a system with ten batteries, the optimum point shifts to a higher temperature set point (-12.5 °C) although remaining at the maximum pump frequency. The reduced temperature set point, reduces the chiller energy while it increases the pump energy by increasing the charging time. Decreasing the pumping power by decreasing the frequency is not beneficial since the personnel cost is still dominant over the pumping energy cost. The total cost contour for this case is shown in Fig. 8.

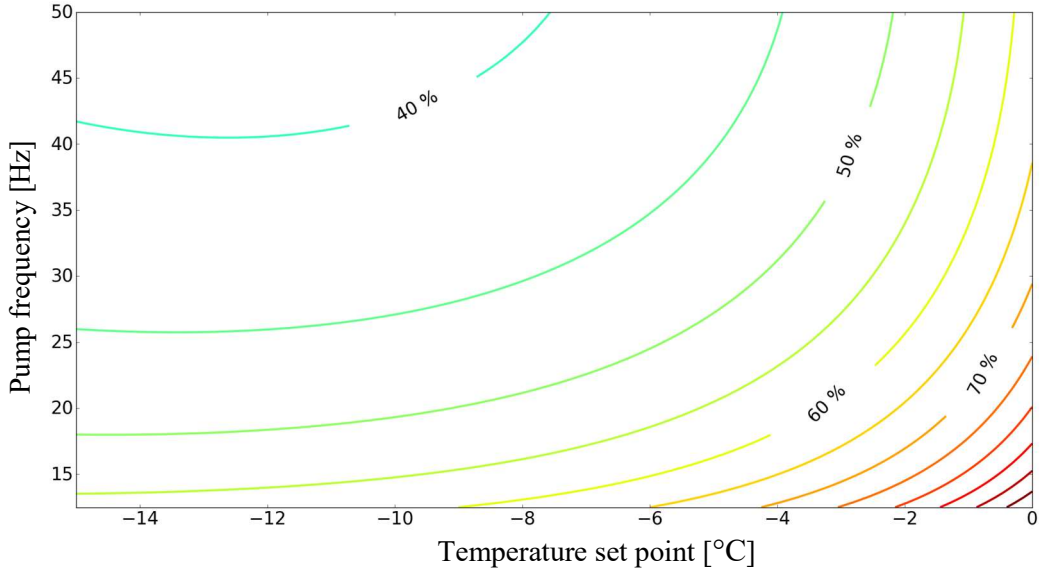


*Fig. 8: Contour of the total cost of a battery system with ten battery expressed as a percentage of the maximum value as a function of temperature set point and pump frequency.*

For loading times lower than the waiting time of the zero waiting time optimum, the optimum does not shift. When the waiting time becomes longer, the optimum point will be close to the point where there is no loading time. However, the savings attainable by changing the set points are about 10 %

of the maximum cost. Although the personnel cost is still dominant over the energy cost, optimization requires finding a balance between both costs.

**Case III: 100 batteries**

In the case one hundred batteries are included in a single system, the energy cost is about 62 % of the total cost in the optimum point. The optimum point has shifted to higher inlet temperatures (-2.4 °C) and lower pump frequencies ( 25.5 Hz). If loading time is taken into account, the optimum will shift if the loading time is higher than the waiting time at -2.4 °C and 25.5 Hz. Fig. 9 shows the total cost contour in this case.

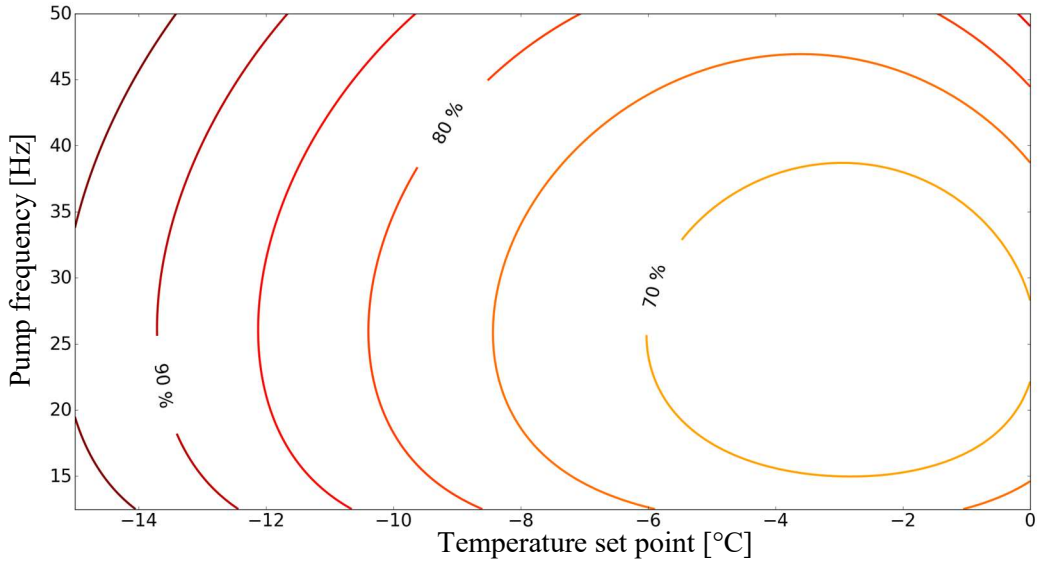


*Fig. 9: Contour of the total cost of a battery system with a single battery expressed as a percentage of the maximum value as a function of temperature set point and pump frequency.*

## 4. Conclusions

The present article discusses a thermal battery for cold chain transport. The charging battery is experimentally characterized for a variety of pump frequencies and inlet temperature set points. The charging time can be correlated as an inverse function of the temperature difference between the temperature set point and the PCM phase change temperature. Secondly an economic model is developed to determine the charging cost per cycle including both the energy cost and the cost of idling a driver. For small systems, the energy cost is insignificant and therefore the charging time should be minimized. Optimizing in this case does not give high benefits. For large systems, the energy cost is important. Optimizing the charging time in this case can reduce the total costs by about 30 % per cycle.

# Nomenclature

| Symbol | Description | Unit |
|---|---|---|
| $\Delta P$ | Pressure drop | Pa |
| $\Delta P_{base}$ | Pressure drop of the base | Pa |
| $\varepsilon_{t_c}$ | Error on the charging time | s |
| $\eta_{pump}$ | Pump efficiency | |
| $\eta_{motor}$ | Pump electrical motor efficiency | |

| | | |
|---|---|---|
| $c_{p,alu}$ | Specific heat aluminum | J/kgK |
| $c_{p,HTF}$ | Specific heat heat transfer fluid | J/kgK |
| $c_{tot}$ | Total cost | € |
| $E_{bat}$ | Battery energy | J |
| $E_{chiller}$ | Chiller energy | J |
| $E_{pump}$ | Pump energy | J |
| $E_{tot}$ | Total energy | J |
| $h_{lat,PCM}$ | Latent heat | J/kg |
| $m_{alu}$ | Mass of the aluminum | kg |
| $m_{HTF}$ | Mass of the heat transfer fluid | kg |
| $m_{PCM}$ | Mass of the phase change material | kg |
| $n_{base}$ | Rotational speed of the base curve | rpm |
| $n_f$ | Rotational speed of the induction motor | rpm |
| $n_{bat}$ | Number of batteries | - |
| $p_e$ | Price of electricity | €/J |
| $p_h$ | Wage of driver | €/s |
| $q$ | Volume flow rate | $m^3/s$ |
| $s$ | Rotor slip | |
| $t_c$ | Charging time | s |
| $t_e$ | time where in and outlet temperatures are not significantly different | s |
| $t_l$ | Loading or unloading time | s |
| $T_{amb}$ | Ambient temperature | °C |
| $T_{ini}$ | Initial temperature | °C |
| $T_{set}$ | Set point temperature | °C |
| $T(s)$ | Torque as a function of rotor slip | Nm |
| $PCM$ | Phase change material | |
| $HTF$ | Heat transfer fluid | |
| $COP_{real}$ | Real coefficient of performance | |
| $COP_{Carnot}$ | Carnot coefficient of performance | |

## Acknowledgments

Wim Beyne received funding from a Ph.D. fellowship strategic basic research of the Research Foundation - Flanders (FWO) (1S08317N). This research was supported by Flanders Make, the strategic research centre for the manufacturing industry, Belgium.

## References

[1] (2012, 03/02). *Improving Cold storage Equipment in Europe*. Available: https://ec.europa.eu/energy/intelligent/projects/en/projects/ice-e

[2] M. Axell and P. Fahlén, "Climatic influence on display cabinet performance," in *IIR Commission D1/B1 Supermarket refrigeration*, 2002.

[3] S. Tassou, G. De-Lille, and Y. Ge, "Food transport refrigeration–Approaches to reduce energy consumption and environmental impacts of road transport," *Applied Thermal Engineering,* vol. 29, pp. 1467-1477, 2009.
[4] M. Liu, W. Saman, and F. Bruno, "Development of a novel refrigeration system for refrigerated trucks incorporating phase change material," *Applied Energy,* vol. 92, pp. 336-342, 2012/04/01/ 2012.
[5] Y. Kozak, M. Farid, and G. Ziskind, "Experimental and comprehensive theoretical study of cold storage packages containing PCM," *Applied Thermal Engineering,* vol. 115, pp. 899-912, 2017/03/25/ 2017.
[6] X. Xu, X. Zhang, and S. Liu, "Experimental study on cold storage box with nanocomposite phase change material and vacuum insulation panel," *International Journal of Energy Research,* vol. 42, pp. 4429-4438, 2018.
[7] Y. Zhao, X. Zhang, and X. Xu, "Application and research progress of cold storage technology in cold chain transportation and distribution," *Journal of Thermal Analysis and Calorimetry,* vol. 139, pp. 1419-1434, 2020/01/01 2020.
[8] M. A. Elliott and G. W. Halbert, "Maintaining the cold chain shipping environment for Phase I clinical trial distribution," *International Journal of Pharmaceutics,* vol. 299, pp. 49-54, 8/11/ 2005.
[9] E. Oró, A. de Gracia, and L. F. Cabeza, "Active phase change material package for thermal protection of ice cream containers," *International Journal of Refrigeration,* vol. 36, pp. 102-109, 2013/01/01/ 2013.
[10] Rubitherm. (24/01). *Organic PCM - RT*. Available: https://www.rubitherm.eu/en/index.php/productcategory/organische-pcm-rt
[11] Temper. (2020, 27/01). *Heat transfer fluid thermal properties*. Available: http://www.temper.se/page/temper/
[12] S. E. Eurostat, "Electricity price statistics," *Electricity prices for non-household consumers. ISSN,* pp. 2443-8219, 2018.
[13] "Collectieve arbeidsovereenkomst van 15 juni 2017," ed. Brussel: Paritair comité voor het vervoer en de logistiek 1400.
[14] G. Zweifel, "A simple chiller model for hourly time step applications," in *Eleventh international IBPSA conference*, 2009.
[15] Grundfoss. (2020, 28/01/2020). *Grundfoss Product Center CR 3-22 A-FGJ-A-E-HQQE-96083190*. Available: https://product-selection.grundfos.com/
[16] S. Kakac, H. Liu, and A. Pramuanjaroenkij, *Heat exchangers: selection, rating, and thermal design*, Third ed.: CRC press, 2012.